

# Albumin-based therapeutics capable of glutathione consumption and hydrogen peroxide generation for synergetic chemodynamic and chemotherapy of cancer

Yang, Guangbao; Wang, Dongdong; Phua, Fiona Soo Zeng; Bindra, Anivind Kaur; Qian, Cheng; Zheng, Rui; Cheng, Liang; Liu, Guofeng; Wu, Hongwei; Liu, Zhuang; Zhao, Yanli

2022

Yang, G., Wang, D., Phua, F. S. Z., Bindra, A. K., Qian, C., Zheng, R., Cheng, L., Liu, G., Wu, H., Liu, Z. & Zhao, Y. (2022). Albumin-based therapeutics capable of glutathione consumption and hydrogen peroxide generation for synergetic chemodynamic and chemotherapy of cancer. *ACS Nano*, 16(2), 2319-2329.  
<https://dx.doi.org/10.1021/acsnano.1c08536>

<https://hdl.handle.net/10356/156675>

<https://doi.org/10.1021/acsnano.1c08536>

---

This document is the Accepted Manuscript version of a Published Work that appeared in final form in *ACS Nano*, copyright © American Chemical Society after peer review and technical editing by the publisher. To access the final edited and published work see <https://doi.org/10.1021/acsnano.1c08536>.

*Downloaded on 20 Mar 2024 19:15:04 SGT*

# Albumin-Based Therapeutics Capable of Glutathione Consumption and Hydrogen Peroxide Generation for Synergetic Chemodynamic and Chemotherapy of Cancer

*Guangbao Yang,<sup>†</sup> Dongdong Wang,<sup>†</sup> Soo Zeng Fiona Phua,<sup>†</sup> Anivind Kaur Bindra,<sup>†</sup> Cheng Qian,<sup>†</sup> Rui Zhang,<sup>‡</sup> Liang Cheng,<sup>‡</sup> Guofeng Liu,<sup>†</sup> Hongwei Wu,<sup>†</sup> Zhuang Liu,<sup>‡\*</sup> Yanli Zhao<sup>†\*</sup>*

<sup>†</sup>Division of Chemistry and Biological Chemistry, School of Physical and Mathematical Sciences, Nanyang Technological University, 21 Nanyang Link, 637371, Singapore.

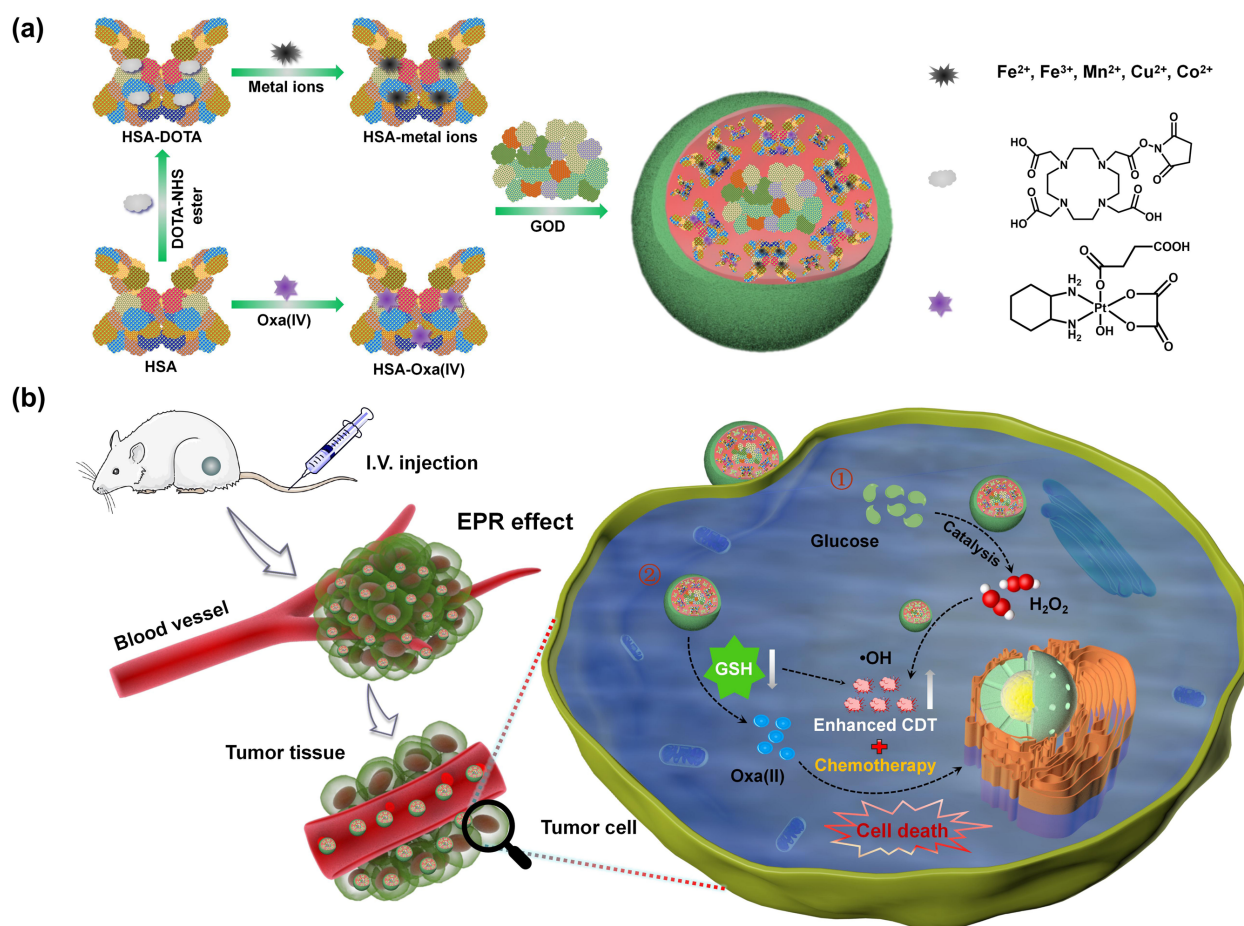
<sup>‡</sup>Institute of Functional Nano & Soft Materials (FUNSOM), Jiangsu Key Laboratory for Carbon-Based Functional Materials & Devices, Soochow University, 199 Ren'ai Road, Suzhou, 215123, Jiangsu, China.

**ABSTRACT:** A nanoscale therapeutic system with good biocompatibility was facilely fabricated by the co-assembly of human serum albumin and glucose oxidase (GOD), where the former being pre-treated with metal ions through a chelating agent or a chemotherapeutic prodrug oxaliplatin (Oxa(IV)). Among different chelating metal ions used, Mn<sup>2+</sup> ion was selected to produce hydroxyl radical (•OH) efficiently through Fenton-like reaction, while GOD loaded in the system was able to generate a large amount of hydrogen peroxide for promoting efficient conversion into highly toxic •OH. In the meanwhile, the conversion of the Oxa(IV) prodrug into chemotherapeutic Oxa(II) was beneficial for the consumption of glutathione, thereby enhancing the chemodynamic therapy (CDT) efficacy. Based on the combined chemotherapy and CDT, the treatment with this system leads to superior antitumor outcome.

**KEYWORDS:** chemodynamic therapy; chemotherapy; glucose oxidase; glutathione; human serum albumin.

Reactive oxygen species (ROS), such as singlet oxygen, hydroxyl radical ( $\bullet\text{OH}$ ), and hydrogen peroxide ( $\text{H}_2\text{O}_2$ ), and can effectively kill tumor cells by damaging biomolecules including DNA strands and proteins in cells.<sup>1-5</sup> One of the emerging developments on ROS-based tumor therapeutics is chemodynamic therapy (CDT), where endogenous  $\text{H}_2\text{O}_2$  is transformed into highly oxidative  $\bullet\text{OH}$  by iron-based Fenton or Fenton-like reactions to ultimately induce intracellular oxidative stress.<sup>6-10</sup> CDT not only overcomes the limitations of cancer phototherapy such as the phototoxicity and penetration depth, but also provides more options for alternative tumor treatment.<sup>11-14</sup> In addition to several iron-based nanosystems (*i.e.*,  $[\text{FeO}(\text{OH})_n]$ , Fe oxides, and  $\text{M}(\text{Sn}, \text{Mn})\text{Fe}_2\text{O}_4$ ) reported as CDT agents, other transition metal species, including  $\text{Mn}^{2+}$ ,  $\text{Co}^{2+}$ , and  $\text{Cu}^{2+}$ , can also be used as catalytic ions.<sup>15-18</sup> Therefore, an universal approach to systematically study catalytic effects of these metal ions for CDT is required.<sup>19-21</sup>

Some studies reported increased efficiency of CDT by depleting the amount of glutathione (GSH), increasing the concentration of  $\text{H}_2\text{O}_2$ , and integrating with prodrugs.<sup>22,23</sup> GSH acts as an central role in protecting cells against a variety of oxidizing species, and thus exhibits high scavenging effect on  $\bullet\text{OH}$  produced by CDT agents.<sup>24</sup> Therefore, down-regulating the level of intracellular GSH is an exciting way to increase effective  $\bullet\text{OH}$  amount.<sup>25</sup> On the other hand, it is a matter of concern that the  $\text{H}_2\text{O}_2$  content inside the tumor cells is very low, and insufficient to catalyze the production of abundant  $\bullet\text{OH}$  by metal ions.<sup>26</sup> Based on this background, it is definitely desirable to achieve a versatile nanosystem that can effectively reduce the content of GSH, while concomitantly increasing the  $\text{H}_2\text{O}_2$  concentration to increase the CDT efficacy.<sup>27,28</sup>



**Scheme 1.** (a) Schematic diagram for the synthesis of HO-HM/GOD nanoparticles. (b) Schematic illustration of HO-HM/GOD-mediated generation of highly toxic  $\cdot\text{OH}$  and activation of Oxa(II) for *in vivo* cancer therapy.

As a major component of Abraxane, that is a clinically employed antitumor nanodrug, human serum albumin (HSA) has been applied as the drug carrier with high biocompatibility to construct a variety of theranostic systems.<sup>29-32</sup> In this work, HSA was pretreated with metal ions through a chelating agent or a chemotherapeutic oxaliplatin (Oxa(IV)) prodrug, together with glucose oxidase (GOD), followed by cross-linking of glutaraldehyde to form a multifunctional nanosystem. The obtained nanosystem has a set of advantages as an intelligent nanoagent for

combination therapy. Natural GOD has the ability to catalyze a large amount of glucose in the tumor to produce abundant  $\text{H}_2\text{O}_2$ , thus increasing the efficacy of the  $\text{Mn}^{2+}$  ion-mediated Fenton-like reaction and facilitating the liberation of highly toxic  $\bullet\text{OH}$ . Specifically, Oxa(IV) could be activated to release toxic Oxa(II) for chemotherapy, which simultaneously consumes intracellular GSH to prevent the scavenging of  $\bullet\text{OH}$ , and realizes synergetic chemo-chemodynamic therapy of cancer.

## RESULTS AND DISCUSSION

The synthetic procedure for the fabrication of the nanosystem is shown in Scheme 1a. A commonly used chelating agent namely 1,4,7,10-tetraazacyclododecane-1,4,7,10-tetraacetic acid mono-*N*-hydroxysuccinimide ester (DOTA-NHS) and a prodrug Oxa(IV)-COOH were first conjugated with HSA to obtain HSA-DOTA and HSA-Oxa(IV) (HO), respectively. On account of strong interactions of DOTA with transition-metal ions, different metal ions, including  $\text{Fe}^{2+}$ ,  $\text{Fe}^{3+}$ ,  $\text{Mn}^{2+}$ ,  $\text{Cu}^{2+}$ , and  $\text{Co}^{2+}$ , were then used to chelate with HSA-DOTA to form HSA-metal complexes.<sup>33,34</sup> At last, GOD, an enzyme that can decompose glucose to  $\text{H}_2\text{O}_2$  rapidly,<sup>35-37</sup> was added with HO and HSA-metal complexes to form the final nanoparticles through cross-linking with glutaraldehyde. After intravenous injection, these nanoparticles can selectively penetrate into the solid tumor and accumulate inside (Scheme 1b).<sup>38,39</sup>

Here, we developed a common method to prepare a range of metal-chelated HSA by mixing different metal ions (*i.e.*,  $\text{Fe}^{2+}$ ,  $\text{Fe}^{3+}$ ,  $\text{Co}^{2+}$ ,  $\text{Mn}^{2+}$ , and  $\text{Cu}^{2+}$ ) with HSA-DOTA. Different HSA-based metal complexes including HSA- $\text{Fe}^{2+}$ , HSA- $\text{Fe}^{3+}$ , HSA- $\text{Mn}^{2+}$  (HM), HSA- $\text{Cu}^{2+}$ , and HSA- $\text{Co}^{2+}$  were successfully formed, all showing an ultra-small size of around 10 nm, as evidenced by transmission electron microscopy (TEM) and dynamic light scattering (DLS) studies (Figure 1a).

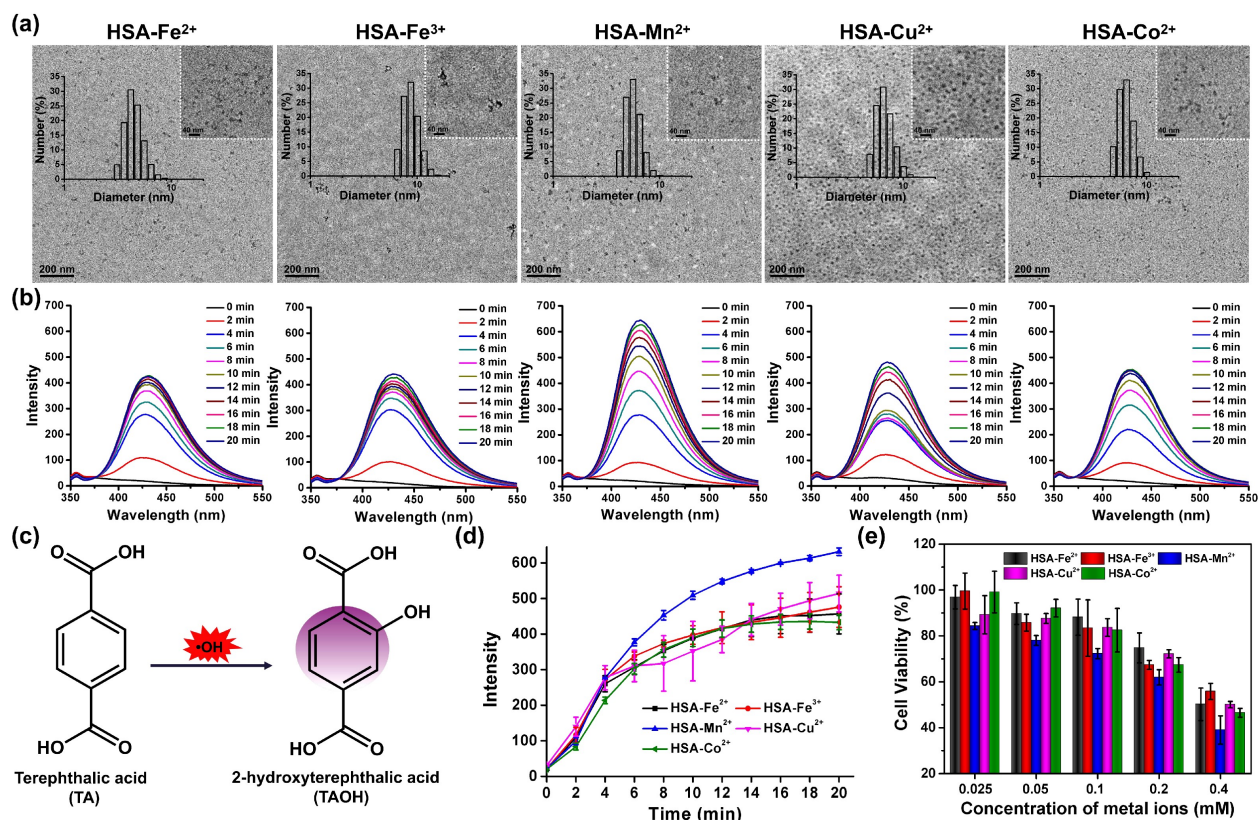


**Figure 1.** (a) TEM images along with DLS-based diameters of different HSA-metal complexes. Inset shows a magnified TEM image. (b) Fluorescence spectra of TAOH enhanced by respective HSA-metal complexes upon the incubation time. (c) Oxidation of nonfluorescent TA to fluorescent TAOH by •OH. (d) Fluorescence intensity changes of TAOH upon the incubation with different HSA-metal complexes in the presence of GOD and glucose. (e) MTT cell viability of different HSA-metal complexes for 24 h. Data were presented as means  $\pm$  standard deviation (s.d.).

We first studied the ability of these HSA-metal complexes for catalytic conversion of H<sub>2</sub>O<sub>2</sub> to •OH. An assay using terephthalic acid (TA) was performed to determine the •OH generation (Figure 1b,c), where TA was oxidized into 2-hydroxyterephthalic acid (TAOH) by •OH, resulting in an increase in the fluorescence.<sup>40</sup> The concentration of •OH production determines the

fluorescence intensity of TAOH. The TA molecule was mixed with different HSA-metal complexes, glucose, and GOD in aqueous solution, showing extraordinarily enhanced emission of resulted TAOH at 426 nm upon the monitoring time, indicating efficient  $\bullet\text{OH}$  generation (Figure 1d). Furthermore, free HSA sample did not show obvious  $\bullet\text{OH}$  production under the same conditions, indicating that coordinated metal ions are one of the essential elements for Fenton-like reaction (Figure S1). The standard MTT (3-(4,5-dimethylthiazol-2-yl)-2,5-diphenyltetrazolium bromide) assay confirmed that these HSA-metal complexes can kill cancer cells more effectively (Figure 1e). Since manganese ion can be employed as an efficient magnetic resonance contrast agent, HM was selected to prepare the final nanoparticles (HO-HM/GOD) for subsequent studies. The  $\bullet\text{OH}$  generated from free  $\text{Mn}^{2+}$  and HM was then monitored by the fluorescence intensity of TAOH (Figure S2). As expected, no appreciable difference in  $\bullet\text{OH}$  production was observed between these two groups.

As revealed by the TEM image, the obtained HO-HM/GOD nanoparticles exhibited a uniform spherical structure (Figure 2a-c). Scanning transmission electron microscope (STEM) mapping images showed the homogeneous distribution of Mn and Pt elements, demonstrating that HO-HM/GOD was successfully synthesized (Figure 2d). Compared to HO and HM nanosystems with the size around 10 nm (Figure 2a,b), HO-HM/GOD showed much larger hydrodynamic size of approximately 140 nm (Figure 2e). Importantly, HO-HM/GOD nanoparticles could be redissolved immediately after the lyophilization without obvious size change (Figure 2f), promoting its long-term storage toward practical applications in the future. HO-HM/GOD nanoparticles can be dispersed well in  $\text{H}_2\text{O}$  and phosphate buffered saline (PBS) without any obvious aggregation after the incubation for 24 h and 7 days respectively, suggesting its excellent stability (Figure S3). The morphology of HO-HM/GOD exhibited no obvious change in PBS after 24 h, suggesting that HO-HM/GOD was stable in the neutral environment (Figure S4a).

Furthermore, the release profile of  $\text{Mn}^{2+}$  from the obtained HO-HM/GOD was quantitatively studied by incubating HO-HM/GOD in PBS for different time intervals. Negligible  $\text{Mn}^{2+}$  was released from HO-HM/GOD, as evidenced by the time-dependent stability of HO-HM/GOD (Figure S4b). The release behavior of  $\text{Mn}^{2+}$  from HO-HM/GOD was then studied in fetal bovine serum (FBS). Approximately 23% of  $\text{Mn}^{2+}$  was released from HO-HM/GOD, indicating that DOTA- $\text{Mn}^{2+}$  in HO-HM/GOD nanoparticles was relatively stable in FBS, possibly due to the enlarged particle size (Figure S5).

Fluorescein isothiocyanate (FITC)-labeled GOD was employed to determine the GOD loading content by recording the FITC fluorescence intensity, which was calculated to be 3.46% in HO-HM/GOD nanoparticles. By using inductively coupled plasma mass spectrometry (ICP-MS), the loading capacity of Oxa(IV) content in HO and HO-HM/GOD was measured to be 3.71% and 1.72%, respectively. The DOTA content in HSA-DOTA was approximately 14.54%. The content of  $\text{Mn}^{2+}$  in HM and HO-HM/GOD was determined to be 1.32% and 0.6%, respectively. However, the  $\text{Mn}^{2+}$  content in HSA- $\text{Mn}^{2+}$  without DOTA conjugation was only 0.27%, indicating that  $\text{Mn}^{2+}$  was chelated with DOTA to form HSA- $\text{Mn}^{2+}$  complex. As a control, a mixture of HM, GOD and untreated HSA without the Oxa(IV) prodrug was used to synthesize HSA-HM/GOD (H-HM/GOD) nanoparticles under the same method, which showed a similar hydrodynamic size to HO-HM/GOD (Figure S6). Another control system, HO-HM without GOD loading, was also acquired by cross-linking of glutaraldehyde.

Since an intracellular reducing environment is needed to promote the release of Oxa(IV) prodrug, we carried out detailed drug release studies in the presence of GSH with different concentrations (Figure 2g).<sup>41,42</sup> Approximately 80% loaded Pt drug was released from the HO-HM/GOD nanoparticles after 48 h incubation with 10 mM GSH solution. In contrast, about 50%

Pt drug was released when HO-HM/GOD was incubated in 2 mM GSH solution, and only about 20% payload was released when incubated in PBS alone.

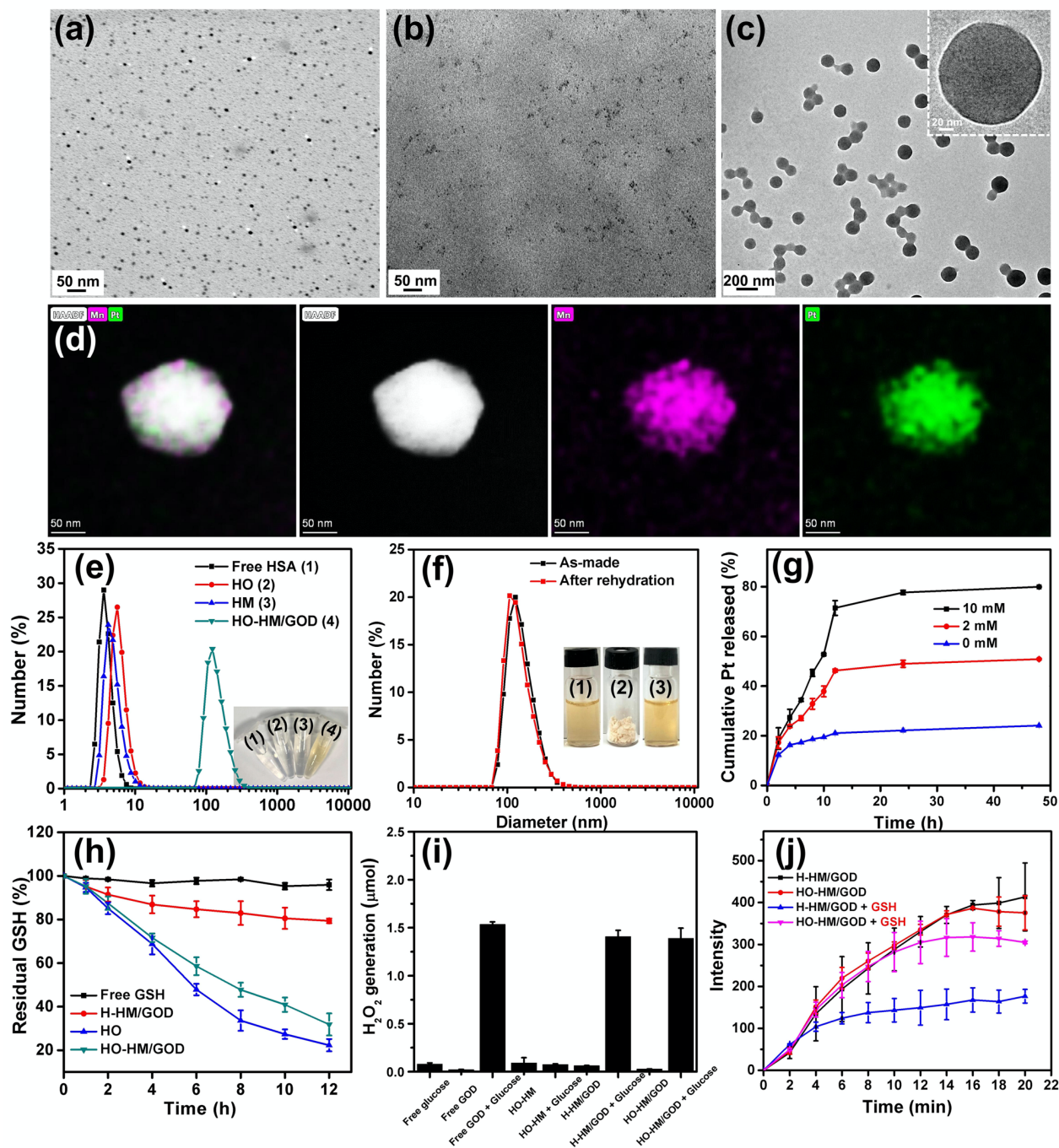


**Figure 2.** TEM images of (a) HO, (b) HM, and (c) HO-HM/GOD nanoparticles. (d) STEM mapping analysis showing the distribution of Mn and Pt elements in the as-synthesized HO-

HM/GOD nanoparticles. (e) DLS sizes and corresponding photographs of (1) free HSA, (2) HO, (3) HM, and (4) HO-HM/GOD nanoparticles dispersed in water. (f) DLS sizes of the as-made HO-HM/GOD and its rehydrated sample after the lyophilization. Inset images are HO-HM/GOD nanoparticles (1) before lyophilization, and (2) after lyophilization, as well as (3) after rehydration. (g) Pt drug release from HO-HM/GOD nanoparticles upon the incubation with GSH at different concentrations. (h) Detection of changes in residual GSH content after the incubation with H-HM/GOD, HO, and HO-HM/GOD for different durations. (i)  $\text{H}_2\text{O}_2$  production in different samples with or without the addition of glucose ( $1 \text{ mg mL}^{-1}$ ). (j) Fluorescence intensity changes of TAOH induced by H-HM/GOD and HO-HM/GOD with or without the GSH addition. Data were presented as mean  $\pm$  s.d.

The inherent ROS scavenging capacity of the overexpressed GSH in cancer cells maintains the intracellular redox balance by eliminating toxic ROS produced by Fenton reaction.<sup>43</sup> Thus, consuming GSH within the tumor microenvironment should be highly useful to increase the therapeutic ability of  $\bullet\text{OH}$  produced from Fenton reaction for enhanced cancer treatment. Since GSH is significantly consumed in the process of reducing Oxa(IV) prodrug to highly toxic Oxa(II), we examined the GSH depletion ability of HO-HM/GOD nanoparticles. Upon increasing the incubation time, the GSH level dropped drastically in the presence of HO or HO-HM/GOD nanoparticles (Figure 2h). However, H-HM/GOD nanoparticles without loading of Oxa(IV) prodrug could not obviously reduce the GSH concentration in solution. We quantitatively determined the  $\text{H}_2\text{O}_2$  amount produced by HO-HM/GOD at  $1 \text{ mg mL}^{-1}$  glucose concentration. Rapidly produced  $\text{H}_2\text{O}_2$  from HO-HM/GOD nanoparticles was observed (Figure 2i), substantiating that HO-HM/GOD nanoparticles were able to maintain high catalytic activity.

Furthermore, GOD loaded in HO-HM/GOD kept 90.5% of its initial activity, without an obvious catalytic ability lose when compared with free GOD in the presence of glucose.

We then investigated the  $\bullet\text{OH}$  generation ability of Fenton-like reaction induced by these nanoparticles in the presence of glucose. As shown in Figures 2j and S7, a significant intensity enhancement was observed when TA was incubated with H-HM/GOD or HO-HM/GOD nanoparticles in  $1\text{ mg mL}^{-1}$  glucose solution, suggesting that highly efficient generation of  $\text{H}_2\text{O}_2$  by GOD loaded nanoparticles could promote the production of a vast amount of  $\bullet\text{OH}$ . Furthermore, HO-HM/GOD nanoparticles could still undergo a high-efficiency Fenton-like reaction to generate  $\bullet\text{OH}$  even after the incubation with GSH. For H-HM/GOD without the Oxa(IV) prodrug, its  $\bullet\text{OH}$  production was severely weakened, owing to the fact that Oxa(IV) prodrug is responsible for the consumption of antioxidant GSH to prevent the  $\bullet\text{OH}$  scavenging.

Intracellular Fenton-like catalytic activity of HO-HM/GOD nanoparticles for  $\bullet\text{OH}$  generation was studied *in vitro*. First, 4T1 murine breast cancer cells were incubated with Cy5.5 labeled HO-HM/GOD nanoparticles for different durations to study the uptake efficacy (Figure S8). Stronger fluorescent signals inside cancer cells were recorded upon the incubation time, indicating efficient uptake of HO-HM/GOD by 4T1 tumor cells. Some studies reported that Pt(IV) can induce the apoptosis and promote the ferroptosis, due to the phospholipid peroxidase glutathione peroxidase 4 (GPX4) inactivation by its effective ability of GSH depletion.<sup>44,45</sup> The intracellular GSH depletion should be attributed to both the Pt(IV) prodrug reduction and the ROS scavenging.<sup>46</sup> Thus, the percentage of intracellular GSH depletion after treated with Pt(IV) prodrug is quite significant. In order to determine the capability of HO-HM/GOD nanoparticles in depleting GSH within cancer cells, the staining assay using thiol tracker violet was conducted. Intracellular GSH was found to be drastically diminished in the groups of HO-HM, HO-HM/GOD, and Oxa(IV) prodrug with higher concentrations (Figure 3a). As a control group, H-

HM/GOD nanoparticles did not show obvious intracellular GSH reduction. A  $\text{H}_2\text{O}_2$  fluorescence assay kit was then used to stain 4T1 cancer cells upon the incubation with free GOD, HO-HM, and HO-HM/GOD in order to examine the  $\text{H}_2\text{O}_2$  production in live cells, respectively (Figure 3b). The green fluorescence was significantly enhanced from free GOD and HO-HM/GOD incubated 4T1 cells, suggesting a large amount of  $\text{H}_2\text{O}_2$  production in these two groups.

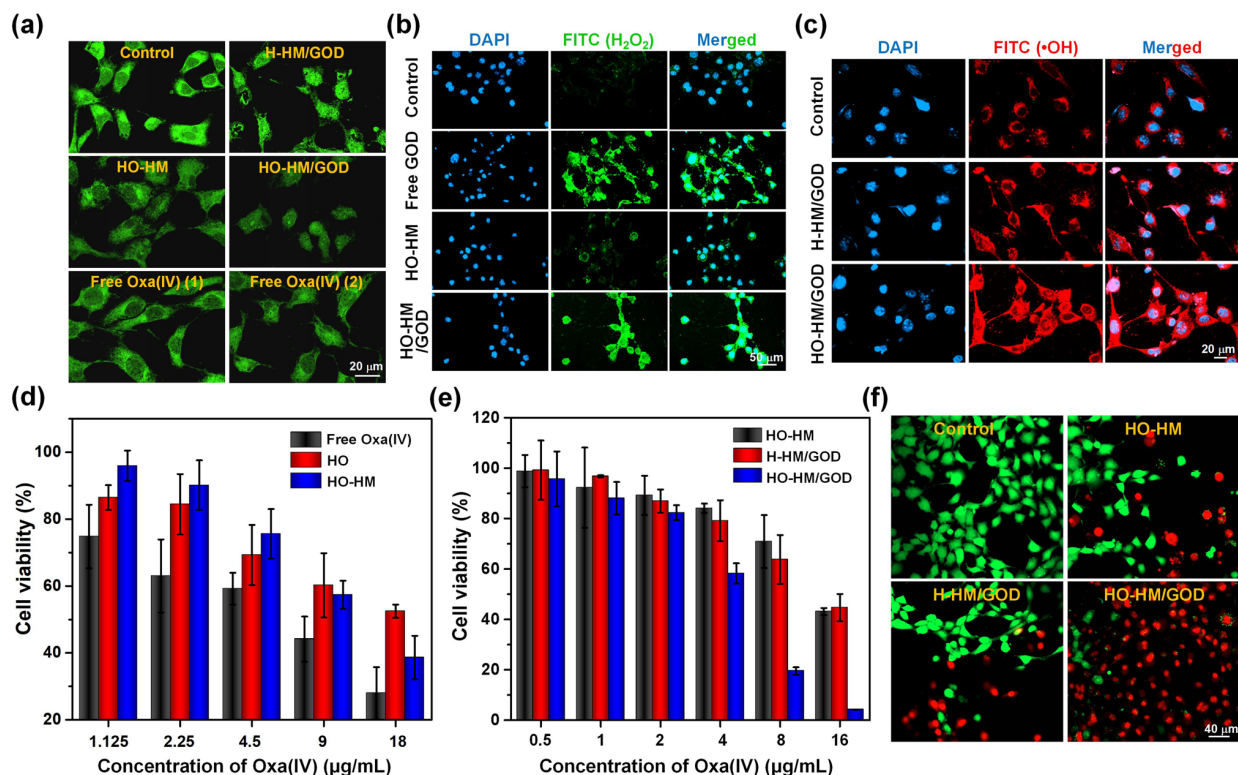


**Figure 3.** (a) Confocal images of thiol tracker violet stained 4T1 cancer cells upon the incubation with H-HM/GOD, HO-HM, HO-HM/GOD, free Oxa(IV) (sample 1, 10  $\mu\text{g mL}^{-1}$ ), and free Oxa(IV) (sample 2, 20  $\mu\text{g mL}^{-1}$ ). (b) Confocal images of 4T1 cancer cells treated with HO-HM, HO-HM/GOD, and free GOD. Green and blue colors indicate  $\text{H}_2\text{O}_2$  and 4',6-diamidino-2-phenylindole (DAPI), respectively.  $\text{H}_2\text{O}_2$  was detected by a  $\text{H}_2\text{O}_2$  fluorescence assay kit. (c) Confocal imaging results of 4T1 cancer cells upon the incubation with H-HM/GOD and HO-HM/GOD, followed by staining with the fluorescence probe APF as  $\bullet\text{OH}$  indicator. (d) Relative

viability of 4T1 cancer cells upon the incubation with free Oxa(IV), HO, and HO-HM nanoparticles at different concentrations. (e) Relative viability of 4T1 cancer cells upon the treatment with HO-HM, H-HM/GOD, and HO-HM/GOD in low glucose medium. (f) Confocal imaging results of Calcein AM/PI co-stained 4T1 cancer cells upon different treatments indicated. Green and red colors indicate live and dead cells, respectively. Data were presented as mean  $\pm$  s.d.

Next, intracellular  $\bullet$ OH generation was carefully tested after the co-incubation of different nanoparticles with  $\bullet$ OH indicator aminophenyl fluorescein (APF). The cells treated with HO-HM/GOD exhibited the strongest intracellular red fluorescence, while the cells treated with H-HM/GOD only displayed limited red fluorescence (Figure 3c). These results collectively demonstrate that HO-HM/GOD nanoparticles not only consume a large amount of GSH, but also produce sufficient  $\text{H}_2\text{O}_2$  for Fenton-like reaction to effectively enhance toxic  $\bullet$ OH content in cancer cells.

In terms of the cell-killing effect of different samples (*i.e.*, free Oxa(IV) prodrug, HO, and HO-HM), even though HO and HO-HM nanoparticles were less toxic than free Oxa(IV) prodrug, they still showed good cell-killing performance (Figure 3d). The combined chemotherapy and CDT were then studied by incubating cells with HO-HM, H-HM/GOD, and HO-HM/GOD nanoparticles, respectively (Figure 3e). The half-maximal inhibitory concentration (IC<sub>50</sub>) of HO-HM/GOD treated group for combination therapy was  $4.33 \mu\text{g mL}^{-1}$ , while the IC<sub>50</sub> of HO-HM group and H-HM/GOD group was  $14.01 \mu\text{g mL}^{-1}$  and  $13.05 \mu\text{g mL}^{-1}$ , respectively. Therefore, the combined treatment by HO-HM/GOD presented the most effective killing effect on 4T1 cells cultured with low glucose concentration medium. Co-staining by Calcein AM/propidium iodide

(PI) was performed to further confirm the effective cancer cell killing (Figure 3f), demonstrating synergistic chemotherapy and CDT achieved by HO-HM/GOD nanoparticles. Furthermore, a similar treatment was conducted on other cancer cell lines (*i.e.*, MCF-7 breast cancer cells and B16F10 melanoma cells), where effective tumor cell destruction was realized by the combined treatment of HO-HM/GOD (Figure S9).

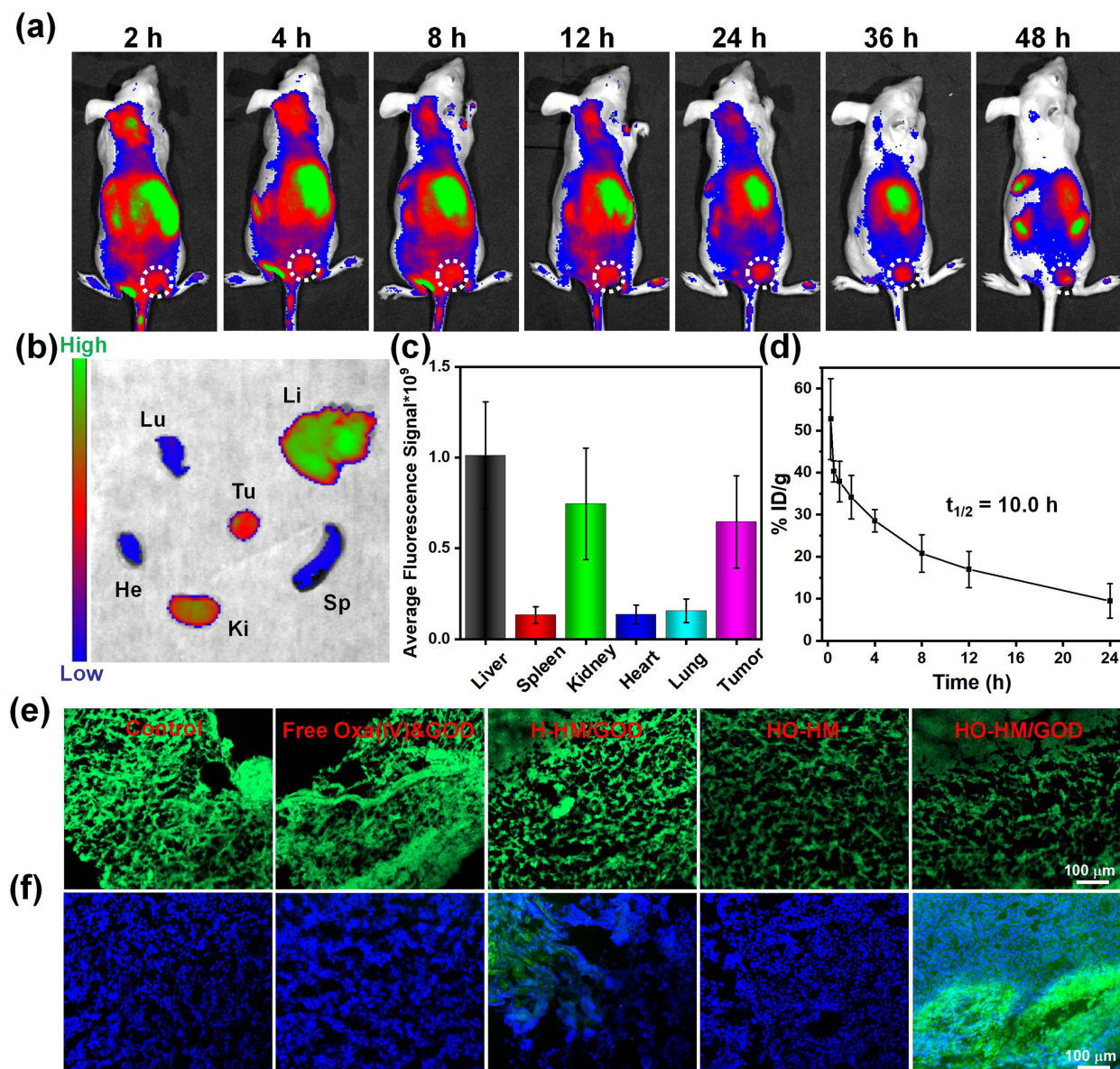


**Figure 4.** (a) Time-dependent fluorescence imaging results of 4T1 tumor-bearing nude mice upon the injection of Cy5.5-labeled HO-HM/GOD nanoparticles. (b) *Ex vivo* fluorescence

imaging results of the major organs taken at 48 h. Tu, Lu, Sp, He, Li, and Ki represent tumor, lung, spleen, heart, liver, and kidney, respectively. (c) Semi-quantification data of *ex vivo* fluorescence imaging results for different organs. (d) Blood circulation half-life (10.0 h) of HO-HM/GOD in mice based on ICP-MS measured Pt levels. (e) Fluorescence imaging results of tumor slices from different treatment groups upon the staining by thiol tracker violet. (f) Fluorescence imaging results of tumor slices stained by DCFH-DA at 24 h post-injection of different agents. Data were presented as mean  $\pm$  s.d.

Next, we performed *in vivo* research on 4T1 tumor-bearing nude mice. The fluorescence imaging of the mice *in vivo* was performed to understand the distribution of Cy5.5 labeled HO-HM/GOD nanoparticles after intravenous injection into mice (Figure 4a). Significant fluorescent signal at the tumor site was found in 48 h, indicating efficient tumor uptake of HO-HM/GOD nanoparticles. This conclusion was also verified by *ex vivo* fluorescence imaging (Figures 4b,c). To quantitatively investigate the properties of HO-HM/GOD nanoparticles *in vivo*, the biodistribution profiles of HO-HM/GOD (Oxa(IV): 5.4 mg kg<sup>-1</sup>) upon intravenous injection into 4T1 tumor-bearing mice were evaluated by measuring the Pt content through ICP-MS. In addition to the high retention in spleen and liver of the mice, a high level of Pt content was also observed in the tumor site after 24 h (Figure S10). Although the content of HO-HM/GOD nanoparticles in blood gradually decreased over time, they still maintained a relatively high level even at 24 h post injection (Figure 4d).

To investigate the ability of the nanosystem for depleting GSH, a GSH staining assay *ex vivo* from these tumor slices after various treatments was conducted. Compared with control, free Oxa(IV)&GOD, and H-HM/GOD groups, weak green fluorescence was recorded in tumor slices from HO-HM and HO-HM/GOD treated mice after intravenous injection, suggesting effective

GSH depletion in the two groups. The results demonstrated that HO-HM/GOD could serve as a GSH depletion system to enhance CDT efficiency (Figure 4e). Then, the ROS staining *in vivo* was performed to evaluate the production of ROS in the tumor upon different treatments. By comparing to the other four groups with relatively low ROS signals, the HO-HM/GOD group exhibited stronger green fluorescence, demonstrating much better ROS production in the tumor site (Figure 4f).

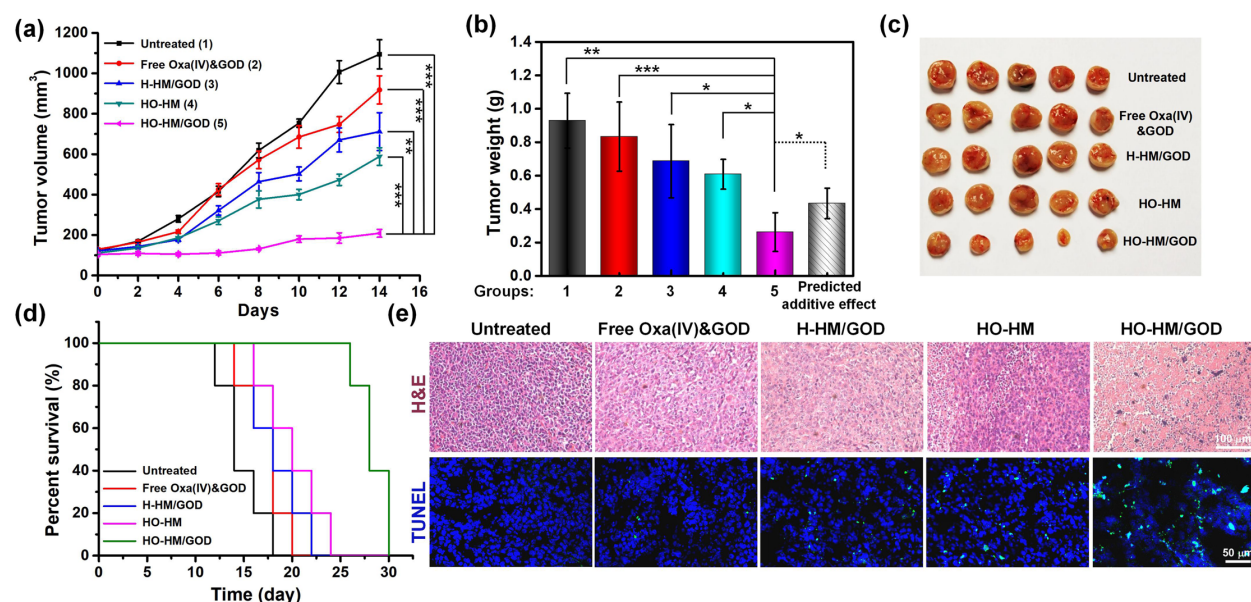


**Figure 5.** (a) Time-dependent growth curves and (b) weights of tumors from different treatment groups after 14 d. The additive effect was calculated through multiplying the tumor inhibition ratio from groups 3 and 4. Error bars in (a) were according to the standard errors of the mean. *P* values were obtained by Tukey's post-test ( $***p < 0.001$ ,  $**p < 0.01$ , or  $*p < 0.05$ ). (c) Photographs of the dissected tumors from the mice upon corresponding treatments. (d) Survival rates of the mice upon different treatments. (e) TUNEL- and H&E-stained histological imaging results from tumor tissues under different groups.

In order to assess the therapeutic efficacy of HO-HM/GOD nanoparticles, 4T1 tumor-bearing nude mice were divided randomly to five treatment groups, *i.e.*, group 1: untreated, group 2: free Oxa(IV)&GOD, group 3: H-HM/GOD, group 4: HO-HM, and group 5: HO-HM/GOD (Oxa(IV): 5.4 mg kg<sup>-1</sup>). To evaluate the antitumor efficiency quantitatively, the tumor volumes were continuously measured for two weeks. While free drug (group 2) was not effective in the suppression of tumor, the tumor growth in the mice administrated with H-HM/GOD (group 3) and HO-HM (group 4) could be partially inhibited (Figure 5a). Importantly, for the mice treated with HO-HM/GOD (group 5), the most significant tumor inhibition was observed as a result of the combination chemotherapy and CDT. As illustrated in Figure 5b,c, tumors treated by HO-HM/GOD had the smallest visible sizes and weights, which were in good agreement with the tumor growth results. In addition, the treatment by HO-HM/GOD nanoparticles was significantly better than the predicted additive effect, indicating the synergistic effect by combining chemotherapy with CDT. The Bliss independent model analysis showed that the observed effect (OE) value (80.93%) was higher than the perceived effect (PE) value (65.03%) in animal studies, further supporting a synergistic effect on the tumor suppression. Moreover, the mice in the treated group of HO-HM/GOD exhibited an obviously prolonged survival time (Figure 5d) as compared to the other four groups, indicating the superiority of the combination therapy (CDT and chemotherapy) over respective monotherapy.

Furthermore, the terminal deoxynucleotidyl transferase-mediated dUTP-biotin nick end labeling (TUNEL) staining and hematoxylin and eosin (H&E) staining on tumor slices after various treatments were performed to observe the tumor cell apoptosis and tumor tissue damage. HO-HM/GOD treated mice showed the highest level of cancer cell apoptosis, while the other groups indicated little or no killing effect on the tumor cells (Figure 5e). Moreover, no obvious change was found in the mouse body weights from all groups throughout the treatment process

(Figure S11), and the treatment by HO-HM/GOD nanoparticles did not result in a noticeable damage to the mouse major organs (Figure S12). Meanwhile, the complete blood panel analysis and the serum biochemistry assay were performed at 12 h, 24 h, 7 d, and 30 d post intravenous injection of HO-HM/GOD nanoparticles. Obviously, all the measured parameters were in the normal ranges, suggesting no obvious side effects induced by HO-HM/GOD nanoparticles (Figure S13 and S14).

To further study the biocompatibility of HO-HM/GOD nanoparticles, mice were injected with nanoparticles four times over seven days (1, 3, 5, and 7 d). One week later, four doses of HO-HM/GOD were further administered on days 15, 17, 19, and 21, respectively. The mice were observed for up to 51 days. No significant change was found in the body weights and organ coefficients as compared with control groups (Figure S15). The H&E staining, complete blood panel analysis, and blood biochemistry assay showed no evident tissue damage, inflammatory lesion, and infection. Thus, it was concluded that HO-HM/GOD had a good biosafety within the tested dosage and timeframe. Furthermore, the maximum tolerated dose (MTD) analysis was performed in Balb/c nude mice (Figure S16). The MTD (weight loss < 15%) was defined without causing major toxicity after the treatment. In the single dose study, it was found that mice in the HO-HM/GOD (Oxa(IV): 21.6 mg kg<sup>-1</sup>) group started to die (2 of 3 mice died), while it was relative safe in the groups of HO-HM/GOD (Oxa(IV): 10.8 mg kg<sup>-1</sup>) and HO-HM/GOD (Oxa(IV): 16.2 mg kg<sup>-1</sup>). Thus, the single MTD for HO-HM/GOD is 3-4 folds higher than that the dose of HO-HM/GOD (Oxa(IV): 5.4 mg kg<sup>-1</sup>) in our animal studies. Meanwhile, we also tested the biosafety of free GOD in healthy nude mice. The body weight measurements, serum biochemistry assay, and complete blood panel analysis were performed (Figure S17 and S18), and no immediate death or no anomalous behavior was observed within 14 days of treatment. These studies indicated that free GOD possessed low toxicity when having the administration

dosage up to 12 mg kg<sup>-1</sup>, a value which was over two times higher than the therapy dosage used. All these results clearly demonstrate the favorable biocompatibility of HO-HM/GOD nanoparticles for therapeutic applications *in vivo*.

## CONCLUSIONS

In summary, a functional nanosystem has been designed by a simple cross-linking strategy for synergetic chemotherapy and CDT of cancer. Different kinds of metal ions were employed to prepare albumin-based nanosystems. Amongst these metal ions, Mn<sup>2+</sup> ion was selected and could efficiently produce •OH by performing Fenton-like reaction. Mn<sup>2+</sup>-containing HO-HM/GOD nanoparticles effectively convert glucose in cancer cells to generate a sufficient amount of H<sub>2</sub>O<sub>2</sub> for the Fenton-like reaction, leading to a significant production of highly toxic •OH. Furthermore, the loaded Oxa(IV) prodrug undergoes a redox reaction in the presence of overexpressed GSH in cancer cells to release the Oxa(II) drug for chemotherapy. Simultaneously, this process enables intracellular GSH depletion to prevent the scavenging of •OH, further enhancing the CDT efficacy. Through the combined chemotherapy and CDT provided by HO-HM/GOD, high antitumor performance on animal models has been achieved. In addition, the albumin-based nanosystem is made up of biocompatible components and the fabrication process is fairly simple. All these features illustrate its promising potential in future practical applications.

## EXPERIMENTAL SECTION

### Synthesis of albumin-based complexes and nanoparticles

HSA-Oxa(IV) (HO) was synthesized according to previously reported protocol.<sup>2</sup> To prepare HSA-DOTA, DOTA (2.2 mg) was dissolved in DMSO (200 µL), which was then dropwise

added into HSA under magnetic stirring in the dark overnight. The solution was ultrafiltered through a centrifugal filter (10 kDa of molecular weight cut-off (MWCO)) for three times. HSA-based complexes with different metal ions, including HSA-Fe<sup>2+</sup>, HSA-Fe<sup>3+</sup>, HSA-Mn<sup>2+</sup>, HSA-Cu<sup>2+</sup>, and HSA-Co<sup>2+</sup>, were prepared following the previously reported method.<sup>34</sup> Different metal compounds, including FeCl<sub>2</sub>, FeCl<sub>3</sub>, MnCl<sub>2</sub>, CuCl<sub>2</sub>, and CoCl<sub>2</sub>, were mixed with HSA-DOTA under a weak alkaline aqueous solution. After overnight stirring, the solution was obtained by the dialysis to remove free metal ions.

To prepare HSA-Oxa(IV)-HSA-Mn<sup>2+</sup>/GOD (HO-HM/GOD) nanoparticles, HO (10 mg mL<sup>-1</sup>), GOD (1 mg), and HM (10 mg mL<sup>-1</sup>) were mixed in aqueous solution (1 mL), followed by adding ethanol (1 mL) slowly. Afterwards, glutaraldehyde (2.5%, 10  $\mu$ L) was introduced into the solution, and the resulted system was stirred at room temperature over 12 h. The control group, HSA-HSA-Mn<sup>2+</sup>/GOD (H-HM/GOD) nanoparticles without the Oxa(IV) prodrug, was obtained with the same method to HO-HM/GOD by replacing HO in the reaction with free HSA. In addition, HSA-Oxa(IV)-HSA-Mn<sup>2+</sup> (HO-HM) without the GOD loading was synthesized by the same procedure except that free HSA (1 mg) was replaced with GOD. To obtain Cy5.5 labeled HO-HM/GOD nanoparticles, Cy5.5 (25  $\mu$ L) in DMSO was added into aqueous solution containing HO-HM/GOD nanoparticles, followed by the incubation for 12 h. After which, the mixture solution was dialyzed against water in the dark overnight to remove free Cy5.5.

### **Drug release experiments**

To investigate the drug release properties, HO-HM/GOD nanoparticles were dialyzed by a dialysis bag (MWCO of 1000 Da) against GSH at different concentrations (0 mM, 2 mM, and 10 mM) in PBS (1 mL) for 48 h. The amount of Pt in the collected solution was measured by ICP-MS.

### **Quantitative analysis of •OH generation, H<sub>2</sub>O<sub>2</sub> production and GSH depletion**

For •OH detection, it was tested based on previously reported method.<sup>40</sup> For different HSA-metal ion complexes, these samples with the same concentration were added into aqueous solution containing GOD, TA (6 mM), and glucose (1 mg mL<sup>-1</sup>). The fluorescence spectra of TA were measured at every 2 min interval. For H-HM/GOD and HO-HM/GOD nanoparticles with or without GSH, they were pre-treated with GSH (0.5 mg mL<sup>-1</sup>) for 12 h, followed by adding them into aqueous solution having HA (6 mM) and glucose (1 mg mL<sup>-1</sup>).

The amount of H<sub>2</sub>O<sub>2</sub> produced by different samples without or with the glucose addition (1 mg mL<sup>-1</sup>) was determined by recording the H<sub>2</sub>O<sub>2</sub> production with titanium oxysulfate (TiOSO<sub>4</sub>) as the indicator by following previously used protocol.<sup>47</sup> Different samples were incubated with glucose for 2 h, followed by measuring the H<sub>2</sub>O<sub>2</sub> concentrations with TiOSO<sub>4</sub> as the indicator.

### **Cellular studies**

4T1 murine breast cancer cells purchased from American Type culture Collection (ATCC) were incubated under 37 °C in 5% CO<sub>2</sub>. The MTT measurements were used to test the cell viability.

For confocal imaging, Cy5.5 labeled HO-HM/GOD nanoparticles were incubated with 4T1 cells for 1 and 4 h, respectively. The samples were labeled with H33342 to reveal the cell nuclei, and imaged under confocal laser scanning microscope (CLSM).

Intracellular H<sub>2</sub>O<sub>2</sub> production was detected by an ab138874 H<sub>2</sub>O<sub>2</sub> assay kit, which can show green fluorescence when reacted with H<sub>2</sub>O<sub>2</sub>. 4T1 cancer cells were incubated with free GOD, HO-HM, and HO-HM/GOD samples for 2 h. After washing the cells by PBS, they were incubated with AbGreen indicator working solution for 30 min. At last, the cells were labeled with DAPI, and then visualized under CLSM.

For testing intracellular amount of GSH, 4T1 cancer cells were cultured with different systems under the same concentration for 12 h, and then stained by thiol tracker violet. The images were recorded by CLSM.

For studying  $\bullet\text{OH}$  production *in vitro*, 4T1 cancer cells were incubated with H-HM/GOD and HO-HM/GOD for 4 h. After washing the cells by PBS, they were incubated with APF-containing media. After labeling with DAPI, the intracellular  $\bullet\text{OH}$  production was examined by measuring the fluorescence of APF under CLSM.

For testing the cell viability of different HSA-metal ion samples, 4T1 cancer cells were seeded into 96-well plates, followed by incubating with HSA- $\text{Fe}^{2+}$ , HSA- $\text{Fe}^{3+}$ , HSA- $\text{Mn}^{2+}$ , HSA- $\text{Cu}^{2+}$ , and HSA- $\text{Co}^{2+}$  nanoparticles under different concentrations for 24 h. The MTT assay was performed to study the cell viability. In terms of chemotherapy, 4T1 cancer cells were incubated with free Oxa(IV), HO, and HO-HM nanoparticles under different concentrations for 60 h.

For the combination therapy, different cell lines (*i.e.*, 4T1 cancer cells, B16F10 melanoma cells, and MCF-7 breast cancer cells) pre-seeded in 96-well cell culture plates with a low glucose cell culture medium were incubated with HO-HM, H-HM/GOD, and HO-HM/GOD nanoparticles under various concentrations in the dark for 24 h, respectively. Afterwards, the MTT assay was performed to study the cell viability. For live/dead assay, 4T1 cancer cells were seeded in 6-well plates with a low glucose cell culture medium and then incubated with HO-HM, H-HM/GOD, and HO-HM/GOD nanoparticles in the dark for 24 h, respectively. The cells were washed with PBS, followed by staining with Calcein-AM (3  $\mu\text{L}$ ) and PI (5  $\mu\text{L}$ ) for 20 min before visualizing under CLSM.

### **Animal studies *in vivo***

Female Balb/c nude mice (6-8 weeks) purchased from Nanjing Peng Sheng Biological Technology Co. Ltd were employed under approved protocols of Soochow University Laboratory Animal Center. The cells ( $1 \times 10^6$ ) in PBS (40  $\mu$ L) were injected subcutaneously onto the right back of mice to obtain the 4T1 tumor model.

For *in vivo* imaging, Cy5.5 labeled HO-HM/GOD nanoparticles (Oxa(IV): 5.4 mg kg<sup>-1</sup>) were injected intravenously into the nude mice. Fluorescence imaging *in vivo* was carried out using an *in vivo* optical imaging system (Lumina, PerkinElmer, Inc.) under different time intervals. To study the biodistribution, three 4T1 tumor-bearing Balb/c nude mice were sacrificed at 24 h after intravenous injection of HO-HM/GOD. Different organs were harvested, weighted, and solubilized by aqua regia. The Pt content in these samples was measured by ICP-MS.

The mice were anesthetized by pentobarbital sodium in the process of animal studies. After the tumor volumes reached  $\sim 100$  mm<sup>3</sup>, 4T1 tumor-bearing nude mice were divided into 5 groups for intravenous injection of different samples: Group 1, Untreated; Group 2, Free Oxa(IV)&GOD; Group 3, H-HM/GOD; Group 4, HO-HM; Group 5, HO-HM/GOD (Oxa(IV): 5.4 mg kg<sup>-1</sup>). The widths and lengths of the tumors and mouse weights were recorded every 2 d over 14 d. The tumor volumes were determined using the following formula for obtaining the tumor growth curves: tumor volume = width<sup>2</sup>  $\times$  length/2. After the treatments, the mice in each group were sacrificed at day 4 to obtain the tumors for TUNEL and H&E staining. The major organs from the untreated and combination therapy groups were processed for H&E staining to study the biocompatibility of these nanosystems. For GSH and ROS staining, the tumor slices were obtained after various treatments at 24 h post-injection, and then stained with thiol tracker violet and DCFH-DA, respectively. For complete blood panel analysis and blood biochemistry assay, healthy Balb/c nude mice were injected with HO-HM/GOD (Oxa(IV): 5.4 mg kg<sup>-1</sup>). The

untreated mice were employed as the control group. The blood samples were obtained for the blood biochemistry and hematology analysis.

The interaction was calculated by the Bliss independent model. The H-HM/GOD inhibited percentage ( $P_B$ ) of tumor growth, and the HO-HM inhibited percentage ( $P_A$ ) of tumor growth were analyzed by the equations  $P_B = (\text{Control} - B) / \text{Control}$  and  $P_A = (\text{Control} - A) / \text{Control}$ , respectively. The theoretical combination inhibition effect (predicted effect, PE) was calculated by:  $PE = P_B + P_A - P_B P_A$ . The observed combined inhibition effect (observed effect, OE) was compared with PE. When  $OE > PE$ , the combination effect is synergistic. When  $OE < PE$ , the combination effect is antagonistic. When  $OE = PE$ , the combination effect is additive.

## ASSOCIATED CONTENT

**Supporting Information.** The Supporting Information is available free of charge on the ACS Publications website.

Materials and characterizations, TEM images, DLS sizes, fluorescence spectra, confocal images, cell viability studies, biodistribution of nanoparticles, body weight changes, H&E stained images, blood biochemistry/complete blood panel analysis, and MTD studies.

## Notes

The authors declare no competing financial interest.

## AUTHOR INFORMATION

### Corresponding Author

\*E-mail: zliu@suda.edu.cn, zhaoyanli@ntu.edu.sg

## ACKNOWLEDGMENTS

This work was supported by the Singapore Agency for Science, Technology and Research (A\*STAR) AME IRG grant (A20E5c0081), the Singapore National Research Foundation Investigatorship (NRF-NRFI2018-03), a Project Funded by the Priority Academic Program Development (PAPD) of Jiangsu Higher Education Institutions, and the Collaborative Innovation Center of Suzhou Nano Science and Technology.

## REFERENCES

1. Dong, Z.; Feng, L.; Chao, Y.; Hao, Y.; Chen, M.; Gong, F.; Han, X.; Zhang, R.; Cheng, L.; Liu, Z. Amplification of Tumor Oxidative Stresses with Liposomal Fenton Catalyst and Glutathione Inhibitor for Enhanced Cancer Chemotherapy and Radiotherapy. *Nano Lett.* **2019**, *19*, 805-815.
2. Yang, G.; Phua, S. Z. F.; Lim, W. Q.; Zhang, R.; Feng, L.; Liu, G.; Wu, H.; Bindra, A. K.; Jana, D.; Liu, Z.; Zhao, Y. A Hypoxia-Responsive Albumin-Based Nanosystem for Deep Tumor Penetration and Excellent Therapeutic Efficacy. *Adv. Mater.* **2019**, *31*, 1901513.
3. Li, J.; Li, Y.; Wang, Y.; Ke, W.; Chen, W.; Wang, W.; Ge, Z. Polymer Prodrug-Based Nanoreactors Activated by Tumor Acidity for Orchestrated Oxidation/Chemotherapy. *Nano Lett.* **2017**, *17*, 6983-6990.
4. Yang, G.; Xu, L.; Xu, J.; Zhang, R.; Song, G.; Chao, Y.; Feng, L.; Han, F.; Dong, Z.; Li, B.; Liu, Z. Smart Nanoreactors for pH-Responsive Tumor Homing, Mitochondria-Targeting, and Enhanced Photodynamic-Immunotherapy of Cancer. *Nano Lett.* **2018**, *18*, 2475-2484.

5. Yao, C.; Wang, W.; Wang, P.; Zhao, M.; Li, X.; Zhang, F. Near-Infrared Upconversion Mesoporous Cerium Oxide Hollow Biophotocatalyst for Concurrent pH-/H<sub>2</sub>O<sub>2</sub>-Responsive O<sub>2</sub>-Evolving Synergetic Cancer Therapy. *Adv. Mater.* **2018**, *30*, 1704833.
6. Lin, H.; Chen, Y.; Shi, J. Nanoparticle-Triggered *in Situ* Catalytic Chemical Reactions for Tumor-Specific Therapy. *Chem. Soc. Rev.* **2018**, *47*, 1938-1958.
7. Zhang, L.; Wan, S.-S.; Li, C.-X.; Xu, L.; Cheng, H.; Zhang, X.-Z. An Adenosine Triphosphate-Responsive Autocatalytic Fenton Nanoparticle for Tumor Ablation with Self-Supplied H<sub>2</sub>O<sub>2</sub> and Acceleration of Fe(III)/Fe(II) Conversion. *Nano Lett.* **2018**, *18*, 7609-7618.
8. Hu, R.; Fang, Y.; Huo, M.; Yao, H.; Wang, C.; Chen, Y.; Wu, R. Ultrasmall Cu<sub>2-x</sub>S Nanodots as Photothermal-Enhanced Fenton Nanocatalysts for Synergistic Tumor Therapy at NIR-II Biowindow. *Biomaterials* **2019**, *206*, 101-114.
9. Qian, X.; Zhang, J.; Gu, Z.; Chen, Y. Nanocatalysts-Augmented Fenton Chemical Reaction for Nanocatalytic Tumor Therapy. *Biomaterials* **2019**, *211*, 1-13.
10. Zhang, C.; Yan, L.; Wang, X.; Dong, X.; Zhou, R.; Gu, Z.; Zhao, Y. Tumor Microenvironment-Responsive Cu<sub>2</sub>(OH)PO<sub>4</sub> Nanocrystals for Selective and Controllable Radiosensitization *via* the X-Ray-Triggered Fenton-Like Reaction. *Nano Lett.* **2019**, *19*, 1749-1757.
11. Liu, C.; Wang, D.; Zhang, S.; Cheng, Y.; Yang, F.; Xing, Y.; Xu, T.; Dong, H.; Zhang, X. Biodegradable Biomimic Copper/Manganese Silicate Nanospheres for Chemodynamic/Photodynamic Synergistic Therapy with Simultaneous Glutathione Depletion and Hypoxia Relief. *ACS Nano* **2019**, *13*, 4267-4277.
12. Liang, R.; Chen, Y.; Huo, M.; Zhang, J.; Li, Y. Sequential Catalytic Nanomedicine Augments Synergistic Chemodrug and Chemodynamic Cancer Therapy. *Nanoscale Horiz.* **2019**, *4*, 890-901.

13. Lin, L.-S.; Huang, T.; Song, J.; Ou, X.-Y.; Wang, Z.; Deng, H.; Tian, R.; Liu, Y.; Wang, J.-F.; Liu, Y.; Yu, G.; Zhou, Z.; Wang, S.; Niu, G.; Yang, H.-H.; Chen, X. Synthesis of Copper Peroxide Nanodots for H<sub>2</sub>O<sub>2</sub> Self-Supplying Chemodynamic Therapy. *J. Am. Chem. Soc.* **2019**, *141*, 9937-9945.
14. Wu, W.; Yu, L.; Jiang, Q.; Huo, M.; Lin, H.; Wang, L.; Chen, Y.; Shi, J. Enhanced Tumor-Specific Disulfiram Chemotherapy by *in Situ* Cu<sup>2+</sup> Chelation-Initiated Nontoxicity-to-Toxicity Transition. *J. Am. Chem. Soc.* **2019**, *141*, 11531-11539.
15. Zhao, P.; Tang, Z.; Chen, X.; He, Z.; He, X.; Zhang, M.; Liu, Y.; Ren, D.; Zhao, K.; Bu, W. Ferrous-Cysteine-Phosphotungstate Nanoagent with Neutral pH Fenton Reaction Activity for Enhanced Cancer Chemodynamic Therapy. *Mater. Horiz.* **2019**, *6*, 369-374.
16. Tang, Z.; Liu, Y.; He, M.; Bu, W. Chemodynamic Therapy: Tumour Microenvironment-Mediated Fenton and Fenton-Like Reactions. *Angew. Chem. Int. Ed.* **2019**, *58*, 946-956.
17. Poyton, M. F.; Sendekci, A. M.; Cong, X.; Cremer, P. S. Cu<sup>2+</sup> Binds to Phosphatidylethanolamine and Increases Oxidation in Lipid Membranes. *J. Am. Chem. Soc.* **2016**, *138*, 1584-1590.
18. Xu, A.; Li, X.; Ye, S.; Yin, G.; Zeng, Q. Catalyzed Oxidative Degradation of Methylene Blue by *in Situ* Generated Cobalt(II)-Bicarbonate Complexes with Hydrogen Peroxide. *Appl. Catal., B* **2011**, *102*, 37-43.
19. Wang, S.; Wang, Z.; Yu, G.; Zhou, Z.; Jacobson, O.; Liu, Y.; Ma, Y.; Zhang, F.; Chen, Z.-Y.; Chen, X. Tumor-Specific Drug Release and Reactive Oxygen Species Generation for Cancer Chemo/Chemodynamic Combination Therapy. *Adv. Sci.* **2019**, *6*, 1801986.
20. Dai, Y.; Yang, Z.; Cheng, S.; Wang, Z.; Zhang, R.; Zhu, G.; Wang, Z.; Yung, B. C.; Tian, R.; Jacobson, O.; Xu, C.; Ni, Q.; Song, J.; Sun, X.; Niu, G.; Chen, X. Toxic Reactive Oxygen

Species Enhanced Synergistic Combination Therapy by Self-Assembled Metal-Phenolic Network Nanoparticles. *Adv. Mater.* **2018**, *30*, 1704877.

21. Li, T.; Zhou, J.; Wang, L.; Zhang, H.; Song, C.; de la Fuente, J. M.; Pan, Y.; Song, J.; Zhang, C.; Cui, D. Photo-Fenton-Like Metal-Protein Self-Assemblies as Multifunctional Tumor Theranostic Agent. *Adv. Healthcare Mater.* **2019**, *8*, 1900192.

22. Ma, B.; Wang, S.; Liu, F.; Zhang, S.; Duan, J.; Li, Z.; Kong, Y.; Sang, Y.; Liu, H.; Bu, W.; Li, L. Self-Assembled Copper-Amino Acid Nanoparticles for *in Situ* Glutathione “AND” H<sub>2</sub>O<sub>2</sub> Sequentially Triggered Chemodynamic Therapy. *J. Am. Chem. Soc.* **2019**, *141*, 849-857.

23. Huo, M.; Wang, L.; Chen, Y.; Shi, J. Tumor-Selective Catalytic Nanomedicine by Nanocatalyst Delivery. *Nat. Commun.* **2017**, *8*, 357.

24. Ding, B.; Shao, S.; Jiang, F.; Dang, P.; Sun, C.; Huang, S.; Ma, P. A.; Jin, D.; Kheraif, A. A.; Lin, J. MnO<sub>2</sub>-Disguised Upconversion Hybrid Nanocomposite: An Ideal Architecture for Tumor Microenvironment-Triggered UCL/MR Bioimaging and Enhanced Chemodynamic Therapy. *Chem. Mater.* **2019**, *31*, 2651-2660.

25. Lin, L.-S.; Song, J.; Song, L.; Ke, K.; Liu, Y.; Zhou, Z.; Shen, Z.; Li, J.; Yang, Z.; Tang, W.; Niu, G.; Yang, H.-H.; Chen, X. Simultaneous Fenton-Like Ion Delivery and Glutathione Depletion by MnO<sub>2</sub>-Based Nanoagent to Enhance Chemodynamic Therapy. *Angew. Chem. Int. Ed.* **2018**, *57*, 4902-4906.

26. Fu, L.-H.; Qi, C.; Hu, Y.-R.; Lin, J.; Huang, P. Glucose Oxidase-Instructed Multimodal Synergistic Cancer Therapy. *Adv. Mater.* **2019**, *31*, 1808325.

27. Tang, Z.; Zhang, H.; Liu, Y.; Ni, D.; Zhang, H.; Zhang, J.; Yao, Z.; He, M.; Shi, J.; Bu, W. Antiferromagnetic Pyrite as the Tumor Microenvironment-Mediated Nanoplatfrom for Self-Enhanced Tumor Imaging and Therapy. *Adv. Mater.* **2017**, *29*, 1701683.

28. Chen, Q.; Luo, Y.; Du, W.; Liu, Z.; Zhang, S.; Yang, J.; Yao, H.; Liu, T.; Ma, M.; Chen, H. Clearable Theranostic Platform with a pH-Independent Chemodynamic Therapy Enhancement Strategy for Synergetic Photothermal Tumor Therapy. *ACS Appl. Mater. Interfaces* **2019**, *11*, 18133-18144.
29. Chen, Q.; Liu, Z. Albumin Carriers for Cancer Theranostics: A Conventional Platform with New Promise. *Adv. Mater.* **2016**, *28*, 10557-10566.
30. Chen, Q.; Wang, X.; Wang, C.; Feng, L.; Li, Y.; Liu, Z. Drug-Induced Self-Assembly of Modified Albumins as Nano-Theranostics for Tumor-Targeted Combination Therapy. *ACS Nano* **2015**, *9*, 5223-5233.
31. Son, S.; Song, S.; Lee, S. J.; Min, S.; Kim, S. A.; Yhee, J. Y.; Huh, M. S.; Chan Kwon, I.; Jeong, S. Y.; Byun, Y.; Kim, S. H.; Kim, K. Self-Crosslinked Human Serum Albumin Nanocarriers for Systemic Delivery of Polymerized siRNA to Tumors. *Biomaterials* **2013**, *34*, 9475-9485.
32. Yang, Z.; Chen, Q.; Chen, J.; Dong, Z.; Zhang, R.; Liu, J.; Liu, Z. Tumor-pH-Responsive Dissociable Albumin-Tamoxifen Nanocomplexes Enabling Efficient Tumor Penetration and Hypoxia Relief for Enhanced Cancer Photodynamic Therapy. *Small* **2018**, *14*, 1803262.
33. Sun, C.; Lin, H.; Gong, X.; Yang, Z.; Mo, Y.; Chen, X.; Gao, J. DOTA-Branched Organic Frameworks as Giant and Potent Metal Chelators. *J. Am. Chem. Soc.* **2020**, *142*, 198-206.
34. Dai, L.; Jones, C. M.; Chan, W. T. K.; Pham, T. A.; Ling, X.; Gale, E. M.; Ratile, N. J.; Tai, W. C.-S.; Anderson, C. J.; Caravan, P.; Law, G.-L. Chiral DOTA Chelators as an Improved Platform for Biomedical Imaging and Therapy Applications. *Nat. Commun.* **2018**, *9*, 857.
35. Zhang, X.; He, C.; Chen, Y.; Chen, C.; Yan, R.; Fan, T.; Gai, Y.; Yang, T.; Lu, Y.; Xiang, G. Cyclic Reactions-Mediated Self-Supply of H<sub>2</sub>O<sub>2</sub> and O<sub>2</sub> for Cooperative Chemodynamic/Starvation Cancer Therapy. *Biomaterials* **2021**, *275*, 120987.

36. Li, J.; Anraku, Y.; Kataoka, K. Self-Boosting Catalytic Nanoreactors Integrated with Triggerable Crosslinking Membrane Networks for Initiation of Immunogenic Cell Death by Pyroptosis. *Angew. Chem. Int. Ed.* **2020**, *59*, 13526-13530.
37. Ke, W.; Li, J.; Mohammed, F.; Wang, Y.; Tou, K.; Liu, X.; Wen, P.; Kinoh, H.; Anraku, Y.; Chen, H.; Kataoka, K.; Ge, Z. Therapeutic Polymersome Nanoreactors with Tumor-Specific Activable Cascade Reactions for Cooperative Cancer Therapy. *ACS Nano* **2019**, *13*, 2357-2369.
38. Fang, J.; Nakamura, H.; Maeda, H. The EPR Effect: Unique Features of Tumor Blood Vessels for Drug Delivery, Factors Involved, and Limitations and Augmentation of the Effect. *Adv. Drug Deliv. Rev.* **2011**, *63*, 136-151.
39. Matsumoto, Y.; Nichols, J. W.; Toh, K.; Nomoto, T.; Cabral, H.; Miura, Y.; Christie, R. J.; Yamada, N.; Ogura, T.; Kano, M. R.; Matsumura, Y.; Nishiyama, N.; Yamasoba, T.; Bae, Y. H.; Kataoka, K. Vascular Bursts Enhance Permeability of Tumour Blood Vessels and Improve Nanoparticle Delivery. *Nat. Nanotechnol.* **2016**, *11*, 533-538.
40. Chang, K.; Liu, Z.; Fang, X.; Chen, H.; Men, X.; Yuan, Y.; Sun, K.; Zhang, X.; Yuan, Z.; Wu, C. Enhanced Phototherapy by Nanoparticle-Enzyme *via* Generation and Photolysis of Hydrogen Peroxide. *Nano Lett.* **2017**, *17*, 4323-4329.
41. Lim, W. Q.; Yang, G.; Phua, S. Z. F.; Chen, H.; Zhao, Y. Self-Assembled Oxaliplatin(IV) Prodrug-Porphyrin Conjugate for Combinational Photodynamic Therapy and Chemotherapy. *ACS Appl. Mater. Interfaces* **2019**, *11*, 16391-16401.
42. Lim, W. Q.; Phua, S. Z. F.; Zhao, Y. Redox-Responsive Polymeric Nanocomplex for Delivery of Cytotoxic Protein and Chemotherapeutics. *ACS Appl. Mater. Interfaces* **2019**, *11*, 31638-31648.
43. Li, J.; Dirisala, A.; Ge, Z.; Wang, Y.; Yin, W.; Ke, W.; Toh, K.; Xie, J.; Matsumoto, Y.; Anraku, Y.; Osada, K.; Kataoka, K. Therapeutic Vesicular Nanoreactors with Tumor-Specific

Activation and Self-Destruction for Synergistic Tumor Ablation. *Angew. Chem. Int. Ed.* **2017**, *56*, 14025-14030.

44. Guo, J.; Xu, B.; Han, Q.; Zhou, H.; Xia, Y.; Gong, C.; Dai, X.; Li, Z.; Wu, G. Ferroptosis: A Novel Anti-Tumor Action for Cisplatin. *Cancer Res. Treat.* **2018**, *50*, 445-460.

45. Zhang, G.; Zhang, L.; Si, Y.; Li, Q.; Xiao, J.; Wang, B.; Liang, C.; Wu, Z.; Tian, G. Oxygen-Enriched Fe<sub>3</sub>O<sub>4</sub>/Gd<sub>2</sub>O<sub>3</sub> Nanopeanuts for Tumor-Targeting MRI and ROS-Triggered Dual-Modal Cancer Therapy through Platinum(IV) Prodrugs Delivery. *Chem. Eng. J.* **2020**, *388*, 124269.

46. Zhu, Z.; Wang, Z.; Hao, Y.; Zhu, C.; Jiao, Y.; Chen, H.; Wang, Y.-M.; Yan, J.; Guo, Z.; Wang, X. Glutathione Boosting the Cytotoxicity of a Magnetic Platinum(IV) Nano-Prodrug in Tumor Cells. *Chem. Sci.* **2016**, *7*, 2864-2869.

47. Zhang, R.; Feng, L.; Dong, Z.; Wang, L.; Liang, C.; Chen, J.; Ma, Q.; Zhang, R.; Chen, Q.; Wang, Y.; Liu, Z. Glucose & Oxygen Exhausting Liposomes for Combined Cancer Starvation and Hypoxia-Activated Therapy. *Biomaterials* **2018**, *162*, 123-131.

## Table of Contents Graphic

